Journal of Catalysis 413 (2022) 150–162

Contents lists available at ScienceDirect

Journal of Catalysis

journal homepage: www.elsevier.com/locate/jcat

Defect engineering over Co_3O_4 catalyst for surface lattice oxygen activation and boosted propane total oxidation

Wenjun Zhu [a,b], Xing-bao Wang [c], Chuang Li [a], Xiao Chen [a], Wen-ying Li [c], Zhongmin Liu [b,*], Changhai Liang [a,*]

[a] State Key Laboratory of Fine Chemicals & Laboratory of Advanced Materials and Catalytic Engineering, Dalian University of Technology, Dalian 116024, China
[b] National Engineering Laboratory for Methanol to Olefins, Dalian National Laboratory for Clean Energy, Dalian Institute of Chemical Physics, Chinese Academy of Sciences, Dalian 116023, China
[c] State Key Laboratory of Clean and Efficient Coal Utilization, Taiyuan University of Technology, Taiyuan 030024, China

ARTICLE INFO

Article history:
Received 29 March 2022
Revised 26 May 2022
Accepted 12 June 2022
Available online 20 June 2022

Keywords:
Co_3O_4
Propane oxidation
VOCs removal
Defect engineering
Reactive oxygen species

ABSTRACT

Developing efficient and stable catalyst is crucial for the catalytic removal of volatile organic compounds (VOCs). Herein, we report an effective and versatile surface defect engineering for regulation of surface lattice oxygen species in Co_3O_4 catalyst by alkaline-earth metal doping-etching strategy. The as-synthesized Ca-Co_3O_4-Ac exhibited remarkable catalytic activity and stability in propane oxidation, with high propane oxidation rate (5.65×10^{-7} mol g^{-1} s^{-1}) and turnover frequency (TOF, 2.12×10^{-3} s^{-1}) at 210 °C. Simultaneously, the doping-etching strategy could increase the specific surface area, low-temperature reducibility, and oxygen mobility of Co_3O_4 catalyst. In addition, in situ diffuse reflectance infrared Fourier transform spectroscopy (in situ DRIFTS), density function theory (DFT) calculation, and propane temperature-programmed desorption/surface reaction (C_3H_8-TPD/TPSR) further revealed that active lattice oxygen species induced by doping-etching strategy promoted the propane activation on the catalyst surface. This work offers a deeper understanding of the reactive oxygen species and provides a feasible strategy for the design of efficient catalysts for practical VOCs removal.

1. Introduction

Volatile organic compound (VOCs) emissions have been strictly regulated and prohibited due to their extensive harm to human health and the environment [1,2]. In general, the majority of the emitted VOCs consist of alkanes, alkenes, halogenated hydrocarbons, aldehydes, ketones, aromatics, alcohols, and sulfur/nitrogen containing compounds [3]. Propane, a typical light alkane, gives rise to considerable proportion of VOCs emissions owing to its wide application as raw material for industrial synthesis [3,4]. Up to now, various remediation technologies have been developed and applied for the removal of VOCs [5–7]. Catalytic oxidation is considered to be one of the best terminal techniques for completely converting VOCs into CO_2 and H_2O [8]. Due to the structural stability of propane, it is necessary to develop and design more efficient and durable catalysts for its total oxidation [9]. Generally, noble metal catalysts show high catalytic performance in propane oxidation, but high cost, low thermal stability and poisoning tendency limit their wide application [10–12]. Therefore, there is an urgent need to explore cost-effective and alternative catalysts for propane oxidation.

According to former reports, transition metal oxides are considered as promising alternatives to noble metal catalysts in propane oxidation [13]. Co_3O_4, as a well-known transition metal oxide, has received enormous attention owing to its excellent redox properties, abundance and low-cost [14,15]. Recently, considerable work has been devoted to fine-tune and precisely control the properties of Co_3O_4, such as morphologies [16,17], specific surface areas [18], exposed crystal planes [19,20], and elements doping [21,22], to improve its catalytic activity. For example, Jian et al. developed Co_3O_4 catalysts with various morphologies and exposed facets for propane catalytic oxidation, and found that Co_3O_4-R possessed more lattice defects and lower coordination Co atoms in the exposed (1 1 0) facet, which promoted the generation of active oxygen and thus enhanced the catalytic activity [23]. Zhang et al. proposed that the precipitation pH affected the composition of cobalt oxide precursor, as well as the physicochemical properties and catalytic performance of Co_3O_4 [24]. Our research group also achieved some results in this area, and found that Ce doping and morphology regulation could significantly improve the catalytic activity of Co_3O_4 for propane oxidation [17,21].

* Corresponding authors.
E-mail addresses: liuzm@dicp.ac.cn (Z. Liu), changhai@dlut.edu.cn (C. Liang).

https://doi.org/10.1016/j.jcat.2022.06.024
0021-9517/

Compared to the traditional modifications, the surface defect engineering has exclusive advantages in sophisticatedly modulating the number and properties of active sites on the catalyst surface. For example, Li et al. reported a chemical etching method to selectively dissolve A-site cations in ABO_3 perovskites to obtain modified nanomaterials with higher catalytic activities, such as 3DOM-LMO [25], MnO_2/$LaMnO_3$ [26], and $LaCoO_3$ [27]. However, the existing chemical methods relied on strong acids, which inevitably destroyed the structure and stability of the catalyst, thus restricted their applications in transition metal oxides, especially for Co_3O_4. In order to improve the stability of catalyst and the applicability of chemical etching method, a novel strategy for surface defect engineering is proposed, which takes advantage of the easy solubility of alkaline-earth metals oxides in weak acid. This strategy is to first modulate the surface electronic structure and metal valence state of Co_3O_4 by doping alkaline-earth metals, and then use weak acid etching to induce active sites, which in turn improves the catalytic activity of the catalyst. In addition, the alkaline-earth metals (Mg, Ca, etc.) as additives to Co_3O_4 catalyst are rarely reported, and systematic elucidation of the effects of alkaline-earth metal doping and subsequent acid etching will contribute to the development of other types of transition metal oxides.

In this work, the doping-etching strategy was firstly applied to the synthesis of Co_3O_4 catalyst, and its catalytic activity and stability for propane oxidation were investigated. Various characterizations were performed to explore the physicochemical properties of Co_3O_4 catalyst with alkaline-earth metal doping and the following acid etching, as well as their structure–function relationship in propane oxidation. Concomitantly, the C_3H_8 adsorption and activation on the catalyst surface were investigated by the DFT calculation and C_3H_8-TPD/TPSR experiments. In addition, in-situ DRIFTS analysis was performed to reveal the reaction mechanism of propane oxidation, and the evolution of intermediates due to alkaline-earth metal doping and the following acid etching.

2. Experimental section

All chemicals and reagents were analytical reagent grade and purchased from Sinopharm Chemical Reagent Co., Ltd. The reaction gases, including C_3H_8 (>99.999%), O_2 (>99.999%), Ar (>99.999%), 10 vol% H_2/Ar and other mixed gases were purchased from Dalian Special Gases Co., Ltd. and used without further purification.

2.1. Catalyst preparation

The M−Co_3O_4 (M = Mg, Ca, Co) samples were synthesized by a citric acid sol–gel method, similar to those in [21]. $Co(NO_3)_2{\cdot}6H_2O$ (5.82 g, 20 mmol) and $Mg(NO_3)_2{\cdot}6H_2O$ (0.26 g, 1 mmol) or $Ca(NO_3)_2{\cdot}4H_2O$ (0.24 g, 1 mmol) were dissolved in 60 mL of deionized water. Then, the above solution was stirred with an excess citric acid solution at 60 °C for 1 h. Afterwards, the mixed solution was rotary-evaporated into a viscous substance and dried at 100 °C overnight. Finally, the powder was calcined at 400 °C in O_2/Ar stream for 3 h. The resulting samples were denoted as Co_3O_4, Mg-Co_3O_4, and Ca-Co_3O_4. XCa-Co_3O_4 (X = 1%, 3%, 5%) indicated the different molar ratios of Ca/Co in Ca-Co_3O_4 samples.

In the acetic acid etching process, fresh M−Co_3O_4 sample (0.5 g) was dispersed in 100 mL acetic acid solution (0.1 M) and stirred for 1 h. Then, the suspension was filtered and washed with deionized water to neutral, and dried at 100 °C overnight. The samples were labeled as M−Co_3O_4−Ac. Ca-Co_3O_4-Y (Y = 0.05, 0.1, 0.2 M) denoted that Ca-Co_3O_4 samples were etched by acetic acid solution at these concentrations. The synthesis prodedure of M−Co_3O_4 and M−Co_3O_4−Ac samples is shown in Scheme 1.

2.2. Catalyst characterization

The X-ray diffraction (XRD) was performed on a SmartLab 9KW diffractometer. The metal element composition was determined by inductively coupled plasma-optical emission spectrometer (ICP-OES, Optima 2000DV). The N_2 adsorption–desorption isotherms were measured on a Quantachrome Autosorb-iQ instrument. The X-ray photoelectron spectroscopy (XPS) was performed on Thermo ESCALAB 250. The morphology and nanostructure were obtained by scanning electron microscope (SEM, FEI Nova NanoSEM 450) and transmission electron microscope (TEM, FEI Tecnai G20 F30).

Hydrogen temperature-programmed reduction (H_2-TPR), oxygen temperature-programmed desorption (O_2-TPD), and O_2-pulse chemisorption experiments were performed on Micromeritics AutoChem II 2920 chemisorption analyzer. For H_2-TPR experiment, each sample (50 mg) was pretreated at 200 °C for 1 h in Ar flow (30 mL min^{-1}). Then, the sample was reduced in 10 vol% H_2/Ar flow (30 mL min^{-1}) from room temperature to 600 °C (10 °C min^{-1}). In O_2-TPD experiment, 100 mg of sample was pretreated at 300 °C for 0.5 h in 2 vol% O_2/He flow (30 mL min^{-1}). Then, the sample was purged with a He flow (30 mL min^{-1}) at 50 °C for 1 h, and programmed heating to 600 °C (10 °C min^{-1}). In O_2-pulse chemisorption, 50 mg of sample was firstly pretreated in an oxygen stream (30 mL min^{-1}) for 30 min at 210 °C, and swept with He for 10 min. Then, 10 vol% H_2/Ar (30 mL min^{-1}) was introduced to activate active species, followed by He purged for 10 min. Finally, the experiment was started with a calibrated loop injection of O_2.

Carbon dioxide temperature-programmed desorption (CO_2-TPD) and propane temperature-programmed desorption/surface reaction (C_3H_8-TPD/TPSR) were carried out on a mass spectrograph (GSD 320 OMNISTAR). In a typical CO_2-TPD experiment, 100 mg of sample was pretreated at 200 °C for 1 h in Ar flow (30 mL min^{-1}). Then, the sample was exposed to 10 vol% CO_2/Ar (40 mL min^{-1}) at 40 °C for 1 h and purged with Ar for 1 h. Lastly, the experiment started from 40 to 600 °C under Ar flow (40 mL min^{-1}). The MS signal of CO_2 (m/z = 44) was recorded. C_3H_8-TPD procedure was similar to CO_2-TPD analysis while the adsorption gas was changed to 5 vol% C_3H_8/Ar. C_3H_8-TPSR experiment was conducted with the similar C_3H_8-TPD procedure except the desorption gas of 5 vol% O_2/Ar (40 mL min^{-1}) at the heating process. MS signals of H_2 (m/z = 2), H_2O (m/z = 18), CO (m/z = 28), C_3H_8 (m/z = 43), and CO_2 (m/z = 44) were recorded.

Thermal decomposition of the sample was carried out on a thermogravimetric analyzer (TA SDT-650) coupled with a mass spectrograph (GSD 320 OMNISTAR). About 10 mg samples were loaded into an alumina crucible and heated up to 1000 °C (10 °C min^{-1}) under Ar flow (50 mL min^{-1}). The MS signal of CO_2 (m/z = 44) was recorded.

In situ diffuse reflectance infrared Fourier transform spectroscopy (in situ DRIFTS) were recorded on an FTIR spectrometer (Thermo Fisher Nicolet iS50) with an MCT/A detector and Harrick in situ cell. Before recording the background spectra, the sample (40 mg) was pretreated at 300 °C under 10 vol% O_2/Ar (40 mL min^{-1}) for 1 h. The C_3H_8 adsorption experiment was carried out at 50 °C under 0.2 vol% C_3H_8 (50 mL min^{-1}) flow, while the C_3H_8 oxidation experiment was performed at 50–300 °C in 0.2 vol% C_3H_8, 5 vol% O_2, and Ar balanced atmosphere. All spectra were recorded with 64 scans at a resolution of 4 cm^{-1}.

2.3. Catalytic performance evaluation

The catalytic activity of the catalysts for propane total oxidation was tested using a fixed-bed reactor under atmosphere pressure. For each test, 100 mg of catalyst was diluted with 2 mL of quartz (60–80 mesh) to avoid the hotpots effect. The flow rate of reactant gas (0.2 vol% C_3H_8, 5 vol% O_2, and balanced Ar) was controlled by a

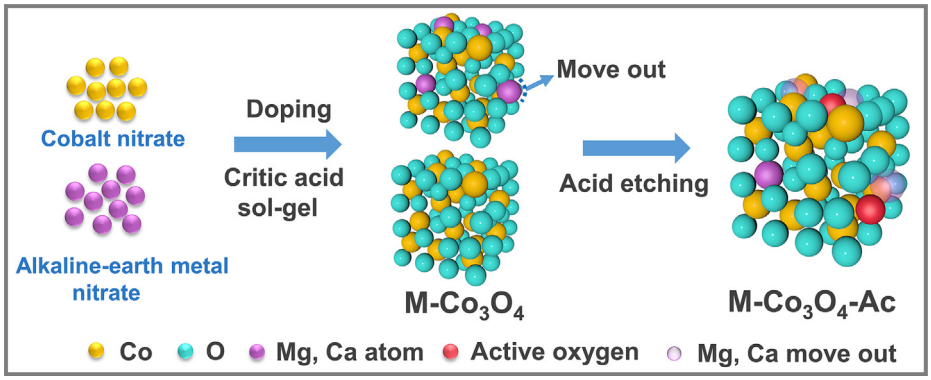

Scheme 1. Synthesis procedure of M−Co_3O_4 and Co_3O_4-Ac samples.

mass flow meter at 200 mL min^{-1}. In some cases, 2.5 vol% H_2O was mixed into the reactant gas. The concentrations of exhaust gas were recorded on an online chromatograph (GC7900) equipped with FID and a mass spectrograph (GSD 320 OMNISTAR). The propane conversion (X_p), specific reaction rate (r_s), and turnover frequency (*TOF*) were calculated as follows:

$$X_p = \frac{C_{p,in} - C_{p,out}}{C_{p,in}} \times 100\% \quad (1)$$

$$r_s = \frac{FX_p}{m_{cat}S_{BET}} \quad (2)$$

$$TOF = \frac{FX_p}{2m_{cat}V_{O_2}} \quad (3)$$

where $C_{p,in}$ and $C_{p,out}$ were the concentration of propane in the inlet and outlet gas, respectively. *F* represented the flow rate of propane (mol s^{-1}), m_{cat} was the mass of catalyst (g), S_{BET} represented the specific surface area (m^2 g^{-1}), and V_{O_2} represented the O_2 uptake of the catalyst (μmol g^{-1}). The number of V_{O_2} was estimated by O_2 pulse chemisorption [28,29], and the TOFs were calculated using the C_3H_8 conversion that was below 20% to exclude the heat or mass transfer limitation. In addition, the mass diffusion transport limitation was checked by the Weisz-Prater criterion [30],

$$N_{W-P} = \frac{-r_A\rho_c R^2}{C_{As}D_e} < 1 \quad (4)$$

The detailed calculation of Weisz-Prater criterion is described in Supplementary Information, and the calculated value of $N_{W\text{-}P}$ in this case is 1.54 × 10^{-3}, which suggested that the mass transfer limitation can be ignored in the activity measurement.

2.4. Computational models and methods

All calculations were performed using the Doml[3] package. The generalized gradient approximation (**GGA**) with the Perdew-Burke-Ernzerhof (**PBE**) function was selected in this study. The calculation parameters were similar to those in previous study [31], as described in Supplementary Information.

3. Results and discussion

3.1. Textural properties of M−Co_3O_4 and M−Co_3O_4−Ac

The XRD patterns of the M−Co_3O_4 and M−Co_3O_4−Ac samples are shown in Fig. 1. For all samples, intense diffraction peaks were observed at 19.0, 31.3, 36.9, 38.5, 44.8, 59.4 and 65.2°, corresponding well to the (111), (220), (311), (222), (400), (422), (511), and (440) planes of spinel Co_3O_4 (PDF#43–1003). The high-purity phase of all samples indicated that the spinel structures of Co_3O_4 were preserved after alkaline-earth metal doping or acid etching treatment. In addition, the alkaline-earth metal doping inhibited the growth of crystallite, as the crystallite size sharply decreased from 22.8 to 20.9 and 14.3 nm after the Mg and Ca introduction (Table 1). However, the crystallite sizes of M−Co_3O_4−Ac sample did not change significantly after the following acid etching, indicating that the primary structure of the M−Co_3O_4−Ac sample remained unchanged during the acid etching process. Meanwhile, ICP-OES analysis demonstrated that most alkaline-earth metals were dissolved during the acid etching treatment, especially for Ca-Co_3O_4 sample, where the Ca/Co molar ratio was 4.6% in the Ca-Co_3O_4 sample and reduced to 0.83% in the Ca-Co_3O_4-Ac sample.

Fig. 2 shows the N_2 adsorption–desorption isotherms and pore size distribution curves of the M−Co_3O_4 and M−Co_3O_4−Ac samples. Obviously, all samples displayed a type-Ⅳ isotherm with an H3 hysteresis loop in the relative pressure (p/p_0) range of 0.6–1.0, which are characteristic of interstitial mesoporous structure formed by the nanoparticle aggregation. It is worth noting that the detection hysteresis of pure Co_3O_4 started at a relative pressure of 0.80 and shifted to a lower p/p_0 value over M−Co_3O_4 samples, implying the progressive change of the textural properties of the M−Co_3O_4 samples upon alkaline-earth metal doping. The textural properties of specific surface area, pore volume and average pore size are shown in Table 1. Compared to that of pure Co_3O_4, the specific surface area and pore volume of Mg-Co_3O_4 and Ca-Co_3O_4 increased from 31 m^2 g^{-1} (0.19 cm^3 g^{-1}) to 46 m^2 g^{-1} (0.22 cm^3 g^{-1}) and 68 m^2 g^{-1} (0.24 cm^3 g^{-1}), respectively, combining with

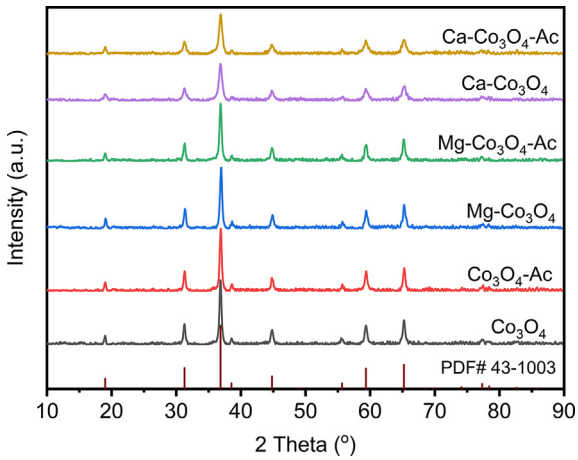

Fig. 1. XRD patterns of the M−Co_3O_4 and M−Co_3O_4−Ac samples.

Table 1
Textural properties and XPS result of M−Co_3O_4 and M−Co_3O_4−Ac samples.

Sample	D_a [a] (nm)	S_{BET} [b] ($m^2\ g^{-1}$)	V [b] ($cm^3\ g^{-1}$)	D_p [b] (nm)	O_2 uptake [c] (μmol g^{-1})	M/Co [d] (%)	Co^{3+}/Co^{2+} [e]	O_α/O_T [e]	O_β/O_T [e]
Co_3O_4	22.8	31	0.19	17.4	75.9	–	0.65	0.055	0.22
Co_3O_4-Ac	22.9	27	0.20	17.4	77.3	–	0.70	0.062	0.23
Mg-Co_3O_4	20.9	46	0.22	12.3	87.0	4.5	0.76	0.15	0.18
Mg-Co_3O_4-Ac	21.2	40	0.22	12.3	100	3.6	0.90	0.063	0.26
Ca-Co_3O_4	14.3	68	0.24	5.6	77.6	4.6	0.85	0.26	0.14
Ca-Co_3O_4-Ac	14.7	61	0.25	6.5	134	0.83	0.97	0.043	0.29

[a] Crystallite sizes calculated by Scherrer formula.
[b] Specific surface area, pore volume and average pore size are obtained from N_2 adsorption/desorption isotherm.
[c] Data obtained from O_2 pulse chemisorption at 210 °C.
[d] Data obtained from ICP-OES.
[e] Data determined from XPS results.

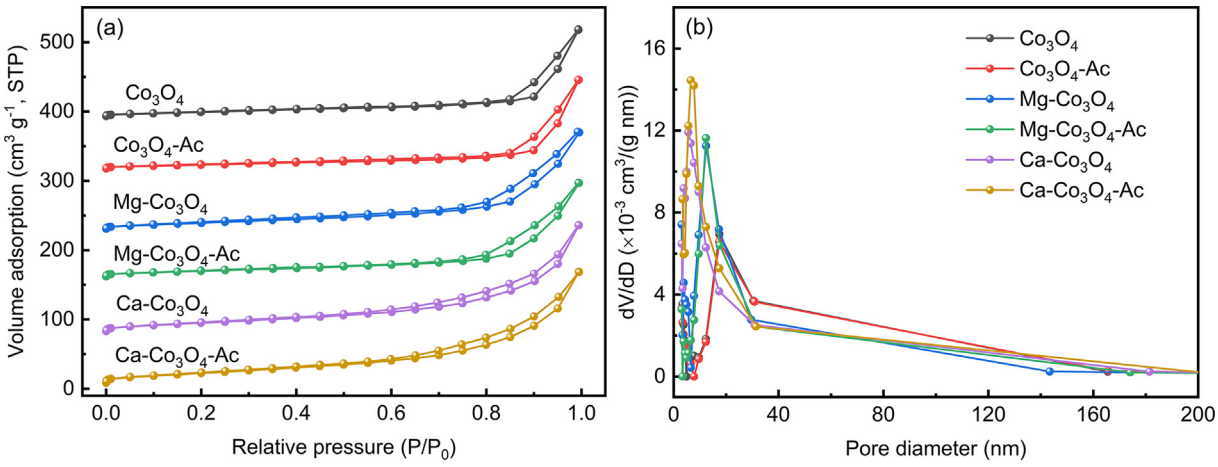

Fig. 2. (a) N_2 adsorption–desorption isotherms, and (b) pore size distribution curves of the M−Co_3O_4 and M−Co_3O_4−Ac samples.

an appropriate minification of the average pore size from 17.4 to 12.3 and 5.6 nm, respectively. In contrast to M−Co_3O_4 samples, the average pore size and pore volume of the corresponding M−Co_3O_4−Ac samples increased slightly, especially for Ca-Co_3O_4-Ac, of which the average pore size and pore volume increased from 5.6 nm and 0.24 $cm^3\ g^{-1}$ to 6.5 nm and 0.25 $cm^3\ g^{-1}$, respectively. Simultaneously, the specific surface areas of Co_3O_4-Ac, Mg-Co_3O_4-Ac, and Ca-Co_3O_4-Ac decreased to 27, 40 and 61 $m^2\ g^{-1}$, respectively. This difference is probably attributed to the etching degree of primary particle and the reconstruction of agglomerates.

The microstructure and morphologies of the samples are shown in Fig. S1 and Fig. 3. All samples featured an irregular shape, and no obvious change occurred with the Ca doping and acetic acid etching (Fig. S1a-c). The analysis of EDS elemental mapping image revealed that Co, O, and Ca were distributed uniformly on the Ca-Co_3O_4 surface (Fig. S1d-g), and the surface Ca content decreased significantly after the following acid treatment (Fig. S1h-k), in accordance with the ICP-OES results. From Fig. 3a and b, the particle sizes of Co_3O_4 was reduced significantly with Ca incorporation, and the average particle size decreased from 27.1 to 13.1 nm, suggesting that the alkaline-earth metal (Ca) inhibited the crystallite growth of Co_3O_4 particles. Moreover, the average particle size of Ca-Co_3O_4-Ac was 13.2 nm (Fig. 3c), similar to that of Ca-Co_3O_4. This suggested that the acid etching treatment did not destroy the primary particle of Ca-Co_3O_4, agreeing with the results calculated by Scherrer formula. In Fig. 3 d-f, the lattice fringes with the interplanar distance of 0.206, 0.246 and 0.290 nm belonged to the (400), (311) and (220) planes of Co_3O_4, respectively, which proved that all samples retained the spinel structure of Co_3O_4. Correspondingly, the lattice fringe of CaO or $CaCO_3$ particles were not detected in the Ca-Co_3O_4 and Ca-Co_3O_4-Ac samples, which was probably due to the amorphism or highly dispersion of CaO or $CaCO_3$ in the Co_3O_4 sample, as verified by XRD.

3.2. Surface chemical properties

The redox properties of M−Co_3O_4 and M−Co_3O_4−Ac samples were investigated by H_2-TPR experiments. As shown in Fig. 4a, the reduction curves of pure Co_3O_4 exhibited three overlapping peaks centered at 280, 340, and 395 °C, respectively. The former peak is usually attributed to the reduction of Co^{3+} to Co^{2+}, and the latter two peaks are ascribed to the reduction of Co^{2+} to metallic Co [17,32,33]. Alkaline-earth metal oxide is known to possess very stable M−O bonds, which are unreducible by hydrogen below 900 °C. Therefore, the main reduction peak of the M−Co_3O_4 samples can be deservedly attributed to the reduction of Co_3O_4. In term of alkaline-earth metals addition, the reduction peaks shifted towards a higher temperature, where the reduction peaks centered at 300 and 440 °C for Mg-Co_3O_4, and at 305, 360, and 450 °C for Ca-Co_3O_4. This indicated that the alkaline-earth metal doping inhibited the reducibility of Co_3O_4. Interestingly, one evident reduction peak appeared below 200 °C for Ca-Co_3O_4, which may be due to the loosely adsorbed surface oxygen anions induced by the surface alkaline-earth metals [34]. After the subsequent acid etching treatment, the redox properties of M−Co_3O_4−Ac were improved, especially for Ca-Co_3O_4-Ac sample, of which the reduction peak temperature downshifted to 275, 340 and 375 °C, while the intensity of reduction peaks increased. As a result, it is reasonable to conclude that alkaline-earth metal doping-etching strategy signif-

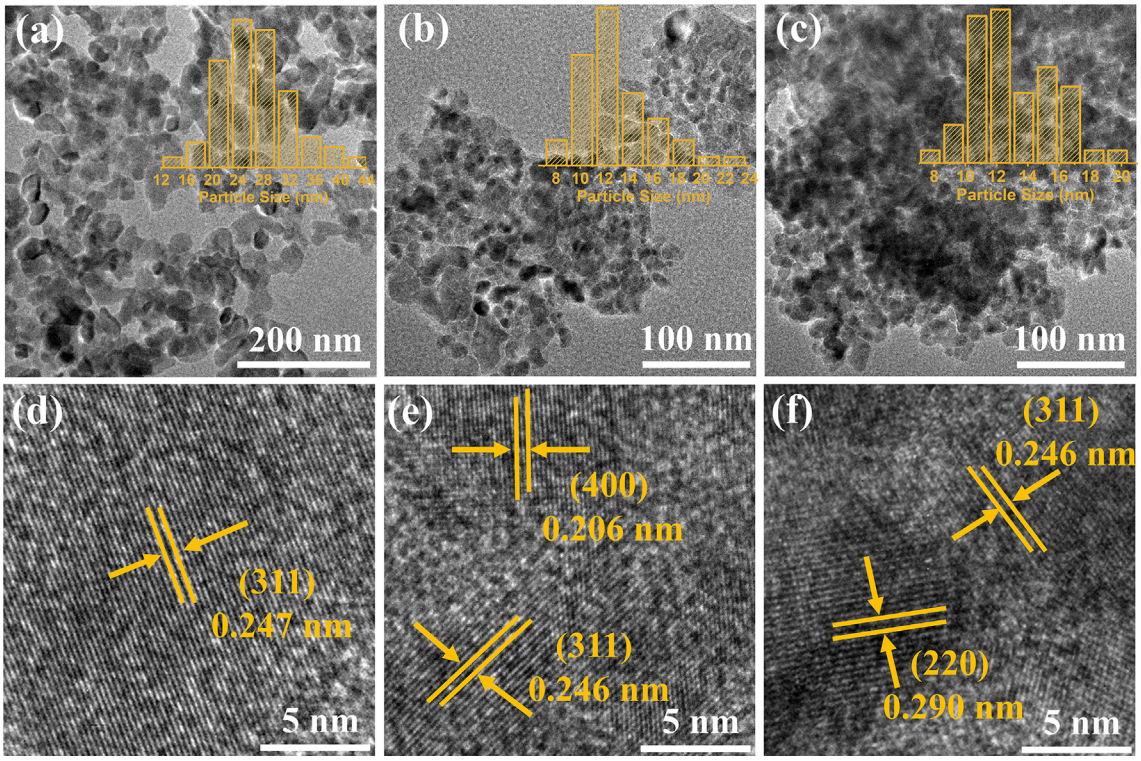

Fig. 3. TEM and HRTEM images of (a, d) Co_3O_4, (b, e) Ca-Co_3O_4, and (c, f) Ca-Co_3O_4-Ac samples.

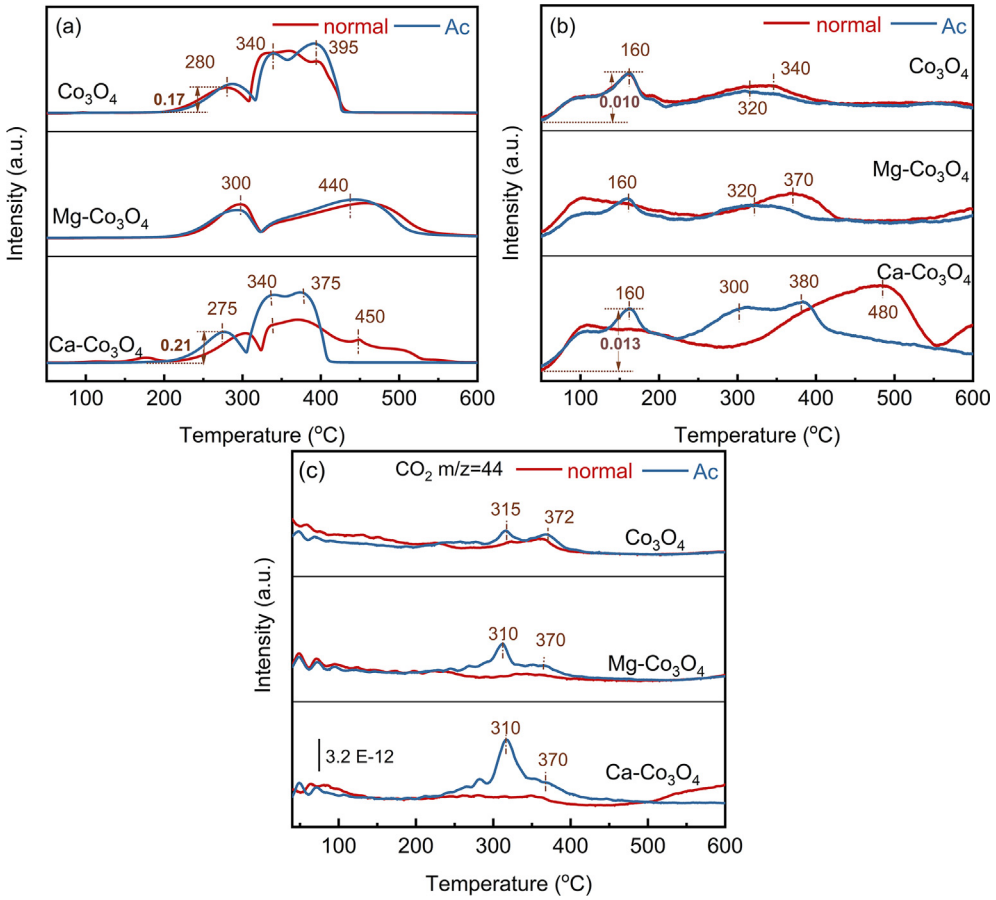

Fig. 4. (a) H_2-TPR, (b) O_2-TPD, and (c) CO_2-TPD profiles of M−Co_3O_4 and M−Co_3O_4−Ac samples.

icantly improve the redox property of Co_3O_4, leading to the enhancement of catalytic cycle in the propane oxidation reaction.

To investigate the properties of oxygen species in the catalysts, O_2-TPD were conducted and the profiles are shown in Fig. 4b. The oxygen species in Co_3O_4 can be assigned to three types: surface adsorbed oxygen species, surface lattice oxygen species and bulk lattice oxygen species [35,36]. Generally, the surface adsorbed oxygen species and surface lattice oxygen species are considered to be the active species in the catalytic oxidation process due to their lower desorption temperature and easy regeneration in oxidizing atmosphere. For pure Co_3O_4, the desorption peaks below 200 °C and at 200–450 °C could be assigned to the surface adsorbed oxygen species and surface lattice oxygen species, respectively [36]. After alkaline-earth metal doping, the desorption peaks at 200–450 °C shifted to a higher temperature, suggesting the inhibition of oxygen mobility and difficult utilization of surface lattice oxygen species. After the subsequent acid etching treatment, the desorption peaks of M−Co_3O_4−Ac was restored to be similar to that of pure Co_3O_4, while the desorption peaks of surface lattice oxygen downshifted to a lower temperature. In particular, Ca-Co_3O_4-Ac exhibited a lower desorption temperature (160 and 300 °C) and a higher desorption peak intensity than Co_3O_4 and Co_3O_4-Ac. This result strongly indicates that doping-etching strategy can increase the oxygen mobility and active oxygen species.

The basicity of Co_3O_4 and M−Co_3O_4−Ac samples was also investigated by CO_2-TPD and shown in Fig. 4c. For pure Co_3O_4, the desorption peak between 200 and 400 °C can be assigned to the CO_2 desorbed at medium basic sites, which is related to the bidentate/-monodentate carbonate (formation by the adsorption of CO_2 on the O bond with Co or unsaturated O) [37]. The CO_2 desorption peak almost disappeared upon addition of alkaline-earth metals, while the CO_2 desorption peak was enhanced after the subsequent acid etching, with the strongest desorption peak of Ca-Co_3O_4-Ac. This indicated that the basic oxygen ions (such as O^-, O_2^{2-} and O_2^-) and surface defects on the surface increased significantly after the alkaline-earth metal doping-etching [23,38]. These basic sites increase the ease to attack the propane molecule in the region with highest electron density and cause its oxidation due to their strong electrophilicity [23,39]. Combined with O_2-TPD result, the oxygen species of Co_3O_4 is blocked by the alkaline-earth metal doping, and more surface defects and active oxygen species generate after the subsequent acid etching treatment.

XPS was carried out to investigate the surface chemical states of the M−Co_3O_4 and M−Co_3O_4−Ac samples. Table S1 shows that the surface M/Co molar ratio of M−Co_3O_4 was higher than the theoretical value, indicating that the alkaline-earth metal was enriched on the M−Co_3O_4 surface. After the subsequent acid treatment, the surface M/Co content decreased significantly, confirming that most of the alkaline-earth metals on the M−Co_3O_4−Ac surface were dissolved. The XPS spectra of Co 2p shows two spin–orbit splitting peaks of Co $2p_{1/2}$ (795.0 eV) and Co $2p_{3/2}$ (780.0 eV), which were deconvoluted into Co^{2+}, Co^{3+}, and two weak satellite peaks [40,41]. The low binding energy peaks at 779.5 and 794.8 eV were attributed to Co^{3+}, and the high binding energy peaks at 781.5 and 797.1 eV were assigned to Co^{2+}. As shown in Table 1, the Co^{3+}/Co^{2+} molar ratio of Co_3O_4 gradually increased after the alkaline-earth metal doping and acid etching treatment. For example, the molar ratio of Co^{3+}/Co^{2+} over Co_3O_4 was 0.65, whereas it severally increased to 0.85 for Ca-Co_3O_4 and 0.97 for Ca-Co_3O_4-Ac. This phenomenon demonstrated that the alkaline-earth metal (Ca, Mg) doping and acetic acid etching treatment favor Co cations in high valence state on the surface.

The O 1 s spectra of M−Co_3O_4 and M−Co_3O_4−Ac samples were fitted into three components (Fig. 5b), which were assigned to lattice oxygen species (O_γ, 529.3–529.8 eV), adsorbed oxygen species (O_β, 530.8–531.1 eV), and surface hydroxyl groups or water (O_α, 532.0 eV), respectively [42]. The shift of O_γ peak for M−Co_3O_4 and M−Co_3O_4−Ac samples indicated that the effective negative charge and electron density of the surface oxygen were changed [43]. Meanwhile, the surface O_α content (O_α/O_T) of the samples obviously increased with the doping of alkaline-earth metal, which could be interpreted as the loosely adsorbed oxygen anions induced by alkaline-earth metal on the surface. Conversely, the O_β content (O_β/O_T) of the samples slightly decreased as the alkaline-earth metals addition, in which the O_β content of Co_3O_4, Mg-Co_3O_4 and Ca-Co_3O_4 were 0.22, 0.18 and 0.14, respectively. The chemisorbed oxygen species is known to have better oxidation activity in the oxides catalyst [36]. Therefore, it can be inferred that the catalytic activity of the Co_3O_4 samples may be restricted by the alkaline-earth metal doping. After the following acid etching, Mg-Co_3O_4-Ac (0.26) and Ca-Co_3O_4-Ac (0.29) had a relative high O_β content on the surface, even higher than that of Co_3O_4-Ac (0.23), suggesting that the existence of more active oxygen species on the M−Co_3O_4−Ac surface. This is in accordance with the O_2-TPD result that the alkaline-earth metal doping-etching strategy enhances the active oxygen species on the surface.

3.3. Catalytic performance

The activities of the M−Co_3O_4, and M−Co_3O_4−Ac catalysts for propane oxidation were evaluated and the results are shown in Fig. 6a. With the doping of alkaline-earth metals, the propane conversion curves of M−Co_3O_4 catalysts shifted to high temperature, where the T_{90} of Co_3O_4, Mg-Co_3O_4 and Ca-Co_3O_4 were 279, 306 and 348 °C, respectively, indicating that alkaline-earth metal doping inhibited the catalytic activity of M−Co_3O_4 catalyst. After the subsequent acid etching treatment, the catalytic activity of M−Co_3O_4−Ac catalyst was improved significantly, and Ca-Co_3O_4-Ac exhibited the best catalytic performance, accompanying with the T_{90} of 260 °C, which was 19 and 88 °C lower than that of Co_3O_4 and Ca-Co_3O_4 catalyst, respectively. This indicated that alkaline-earth metal doping-etching strategy could significantly enhance the catalytic activity of Co_3O_4 catalyst. In particular, Fig. S2 showed that the catalytic activity of Ca-Co_3O_4 catalyst decreased with the incorporation of Ca content, while the subsequent acid etching improved the catalytic activity of Ca-Co_3O_4-Ac to different degrees. This result further confirmed the effectiveness of the alkaline-earth metal doping-etching strategy for improving catalyst activity. Fig. 6b showed that Ca-Co_3O_4-Ac catalyst possessed the lowest activation energy (E_a = 62.6 kJ mol^{-1}) for propane oxidation, notably lower than the E_a values of Ca-Co_3O_4 (88.1 kJ mol^{-1}) and Co_3O_4 (66.9 kJ mol^{-1}). This implied that the alkaline-earth metal doping-etching strategy reduced the E_a required for the propane oxidation. Fig. 6c displayed the retention of good catalytic activity at high GHSV within Ca-Co_3O_4-Ac, which showed potential for practical application under harsh conditions.

For better understanding the intrinsic catalytic activity of the M−Co_3O_4 and M−Co_3O_4−Ac catalysts, the reaction rate, specific surface activity and turnover frequency (TOF) at 210 °C were calculated and listed in Table 2. It was observed that the propane reaction rate of Ca-Co_3O_4-Ac was 5.65 × 10^{-7} mol g^{-1} s^{-1}, almost two times higher than that of Co_3O_4 catalyst (3.55 × 10^{-7} mol g^{-1} s^{-1}). The specific surface activity of Ca-Co_3O_4-Ac catalyst (0.924 × 10^{-8} mol m^{-2} s^{-1}) was also higher than that of Ca-Co_3O_4 (0.0314 × 10^{-8} mol m^{-2} s^{-1}), but a bit lower than Co_3O_4 (1.14 × 10^{-8} mol m^{-2} s^{-1}). Given the differences in specific surface area of Ca-Co_3O_4 (68 m^2 g^{-1}), Ca-Co_3O_4-Ac (61 m^2 g^{-1}) and Co_3O_4 (31 m^2 g^{-1}), it can be inferred that there is a relationship between the specific surface area and the catalytic activity, but it is not the key factor affecting the catalyst activity. In addition, the TOFs of propane oxidation for M−Co_3O_4−Ac catalyst were higher than those of the corresponding M−Co_3O_4 catalyst as expected, but the TOF of Ca-

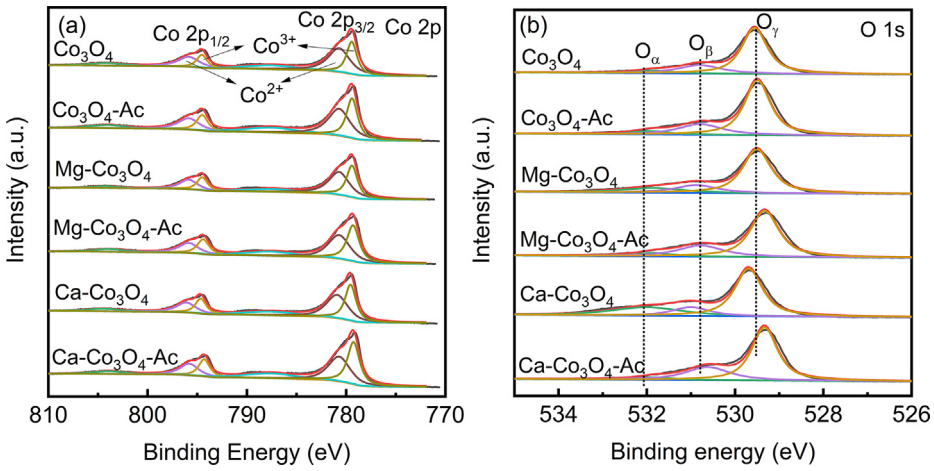

Fig. 5. XPS spectra of (a) Co 2p, (b) O 1 s for the M−Co_3O_4 and M−Co_3O_4−Ac samples.

Co_3O_4-Ac (2.12×10^{-3} s^{-1}) was slightly lower than that of Co_3O_4-Ac (2.38×10^{-3} s^{-1}), which may be due to the fact that the oxygen uptake of Ca-Co_3O_4-Ac (134 μmol g^{-1}) was much larger than that of Co_3O_4-Ac (77.3 μmol g^{-1}). This result suggests that higher catalytic performance of Ca-Co_3O_4-Ac is related to the abundant reactive oxygen species induced by the alkaline-earth metal doping-etching strategy.

Fig. 6d shows the catalytic activity of Ca-Co_3O_4 catalysts etched at different acid concentrations. It is observed that the catalytic performance of Ca-Co_3O_4 was significantly improved after acid etching treatment, and their crystal structures remained in the initial state (Fig. S3). Fig. 6e further shows that the catalytic activity of Ca-Co_3O_4-Ac tended to decrease slightly with increasing acid concentration, which was consistent with the oxygen uptake, suggesting that reactive oxygen species plays a crucial role in the oxidation reaction. The same conclusion can be drawn from Fig. 6f. The reaction rate of the catalyst was consistent with the reactive oxygen species (O_β/O_T and oxygen uptakes), further confirming that the reactive oxygen species is the key factor affecting the catalytic activity. However, Ca-Co_3O_4 presented similar specific surface area as Ca-Co_3O_4-Ac and similar oxygen uptake as Co_3O_4, but its reaction rate was much lower than that of the above catalysts. According to O_2/CO_2-TPD and H_2-TPR results, it is mainly due to the doping of Ca which hinders the oxygen mobility and basic sites, and inhibits the reducibility of the catalyst, thus leading to the poor ability to oxidize propane. All these results demonstrate that the factors such as specific surface area, reactive oxygen species, oxygen mobility and reducibility combine to affect the catalyst activity. In addition, compared with the reported catalysts (Table 3), Ca-Co_3O_4-Ac catalyst exhibited superior catalytic performance in propane oxidation, indicating that the Co_3O_4 catalyst synthesized by the alkaline-earth metal doping-etching strategy presents great potential for practical application in alkanes VOCs removal.

3.4. C_3H_8-TPD/TPSR analysis

C_3H_8-TPD experiment was carried out to investigate the relationship between reactive oxygen species on the sample surface and the oxidation behavior of propane. Noting that CO_2 and C_3H_8 have the same molecular mass (m/z = 44), the MS signal of m/z = 43 refers to C_3H_8, and the signal with m/z = 44 subtracting m/z = 43 refers to CO_2 production. Fig. 7a shows the CO_2 MS signal over Co_3O_4, Ca-Co_3O_4, and Ca-Co_3O_4-Ac samples during C_3H_8-TPD process. It was observed that the CO_2 peak was negligible over Ca-Co_3O_4 in the temperature range of 100–400 °C, whereas Ca-Co_3O_4-Ac showed a larger CO_2 peak than Co_3O_4. According to the O_2-TPD results, the CO_2 production peak formed in 100–400 °C was due to the consumption of active surface lattice oxygen species, which participated in propane oxidation via a Mars-van Krevelen mechanism [22,29]. Therefore, it can be inferred that the alkaline-earth metal doping had a blocking effect on the surface lattice oxygen, which inhibited the C_3H_8 adsorption on Co_3O_4 surface. After the subsequent acid etching treatment, more active lattice oxygen and enhanced oxygen mobility were induced on the surface, which promoted the propane activation on the surface.

The role of gaseous oxygen in oxidation reaction was studied by C_3H_8-TPSR. As shown in Fig. 7b, with the introduction of gaseous O_2, the CO_2 peak temperature in C_3H_8-TPSR was much lower than that in C_3H_8-TPD, indicating that the presence of gaseous oxygen effectively lowered the reaction temperature, and the consumption of reactive oxygen in the catalyst would be replenished by gaseous oxygen. In addition, the CO_2 MS signal of Ca-Co_3O_4-Ac in C_3H_8-TPSR process was much larger than that of Co_3O_4 and Ca-Co_3O_4, which suggested that larger amount of adsorbed C_3H_8 and reactive oxygen species existed on Ca-Co_3O_4-Ac surface. All these results demonstrate that gaseous oxygen plays an essential role in replenishing oxygen species in propane oxidation reaction, and the doping-etching strategy promotes the activation of propane and oxygen species on the catalyst surface.

3.5. DFT calculation

To gain insight into the different phenomenon of C_3H_8 oxidation on Co_3O_4, Ca-Co_3O_4, and Ca-Co_3O_4-Ac samples, DFT calculation was performed. Generally, the activation of the initial C-H bond is thought to be the rate-determining step in the oxidation of alkanes, which has been supported by isotopic substitution experiment [50], kinetic measurement [51] and theoretical studies[52,53]. Besides, the structure of Ca-Co_3O_4 sample was constructed in two models, most of Ca on the surface as $CaCO_3$-Co_3O_4 model, and little Ca substitution into Co_3O_4 lattice as $Ca_xCo_{3-x}O_3$ model, which was inferred from the decomposition of carbonate in TG-MS analysis (as shown in Fig. S4) and above characterizations. For Ca-Co_3O_4-Ac sample, the Co_3O_4-D model represented that most of $CaCO_3$/Ca was etched, inducing lattice defects and more active oxygen species on the surface. Based on these, the heterolytic dissociation process of the first C-H bond of C_3H_8 was simulated to investigate the surface reactivity of Co_3O_4, Ca-Co_3O_4, and Ca-Co_3O_4-Ac catalysts.

Fig. 8 a and b show the initial adsorption structure of C_3H_8 as well as the transition state and final states for its heterolytic disso-

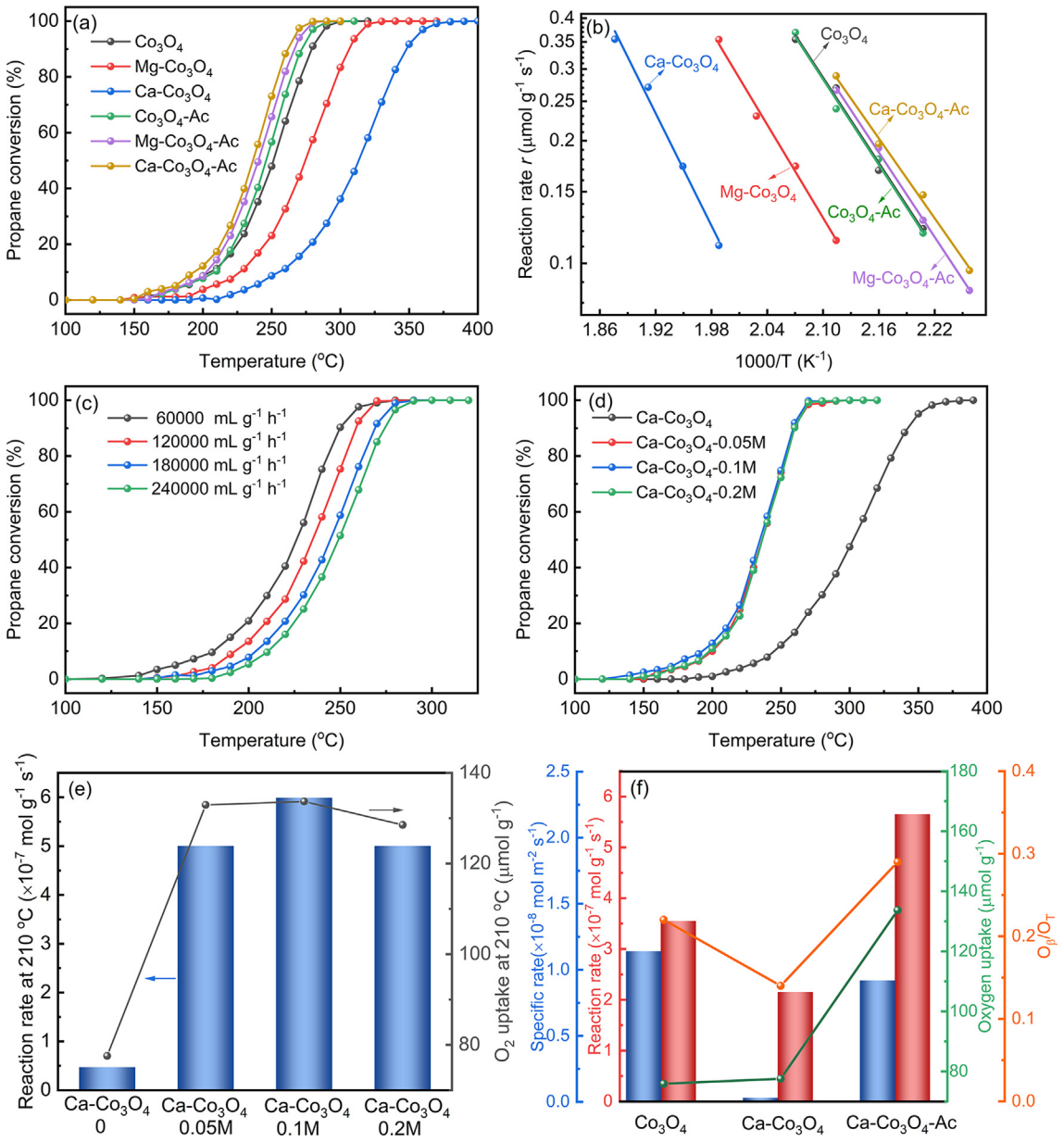

Fig. 6. (a) Propane conversion over M−Co_3O_4 and M−Co_3O_4−Ac catalysts (Reaction conditions: 100 mg catalyst, 0.2 vol% C_3H_8, 5 vol% O_2, and balance Ar, 120000 mL $g^{-1}h^{-1}$). (b) The corresponding Arrhenius plots; a conversion level < 15% was used to make Arrhenius plots and to calculated apparent activation energy. (c) Propane conversion over Ca-Co_3O_4-Ac catalyst at different GHSV, and (d) etched with different acetic acid concentrations (Reaction conditions: 100 mg catalyst, 0.2 vol% C_3H_8, 5 vol% O_2, and balance Ar. Total flow rates: 100–400 mL min^{-1}). (e) The relationship between reaction rates and O_2 uptakes at 210 °C for Ca-Co_3O_4-Y catalysts. (f) The relationship between reaction rates and oxygen species recorded for Co_3O_4, Ca-Co_3O_4, and Ca-Co_3O_4-Ac catalysts.

Table 2
Catalytic activities, reaction rates, TOFs, and activation energy (E_a) of M−Co_3O_4 and M−Co_3O_4−Ac catalysts for propane oxidation.

Catalyst	T_{50} (°C)[a]	T_{90} (°C)[a]	r (×10^{-7} mol g^{-1} s^{-1})[b]	r (×10^{-8} mol m^{-2} s^{-1})[b]	C_3H_8 conversion (%)[b]	TOF (10^{-3} s^{-1})[b]	E_a (kJ mol^{-1})
Co_3O_4	251	279	3.55	1.14	11.2	2.34	66.9
Co_3O_4-Ac	246	271	3.69	1.38	11.7	2.38	67.0
Mg-Co_3O_4	274	306	1.73	0.375	5.70	0.995	73.0
Mg-Co_3O_4-Ac	241	267	4.62	1.15	14.4	2.31	66.3
Ca-Co_3O_4	313	348	0.215	0.0314	0.87	0.139	88.1
Ca-Co_3O_4-Ac	236	260	5.65	0.924	17.3	2.12	62.6

[a] T_{50} and T_{90} are the temperatures for 50% and 90% propane conversion, respectively.
[b] Data obtained at 210 °C.

Table 3
Comparison of the catalytic results of Ca-Co_3O_4-Ac catalyst to those reported in literatures.

Catalyst	Reaction condition	GHSV (mL $g^{-1}h^{-1}$)	T_{50} (°C)	T_{90} (°C)	Conversion (%)	TOF × 10^4 (s^{-1})	Ref.
$LaCo_{0.2}Mn_{0.8}O_3$	0.2 %C_3H_8 + 5 %O_2/Ar	120,000	310	355	16.0(260 °C)	0.58	[7]
LM-EG	0.2 %C_3H_8 + 99.8 %Air	30,000	275	310	15.0(250 °C)	7.60	[44]
SMO-A-HNO_3	0.2 %C_3H_8 + 10 %O_2/N_2	60,000	210	235	14.8(185 °C)	1.59	[9]
SMO-A	0.2 %C_3H_8 + 10 %O_2/N	60,000	270	315	7.0(200 °C)	1.53	[9]
Co_3O_4	0.1 %C_3H_8 + 21 %O_2/He	40,000	229	269	9.4(185 °C)	5.66	[22]
1 %Zr-Co_3O_4	0.1 %C_3H_8 + 21 %O_2/He	40,000	212	241	18.2(185 °C)	9.01	[22]
Pt/Al_2O_3	0.2 %C_3H_8 + 2 %O_2/N_2	80,000	280	350	4.0(200 °C)	21.6	[45]
Ru-Re/γ-Al_2O_3	0.5 %C_3H_8 + 99.5 %Air	60,000	195	270	8.0(170 °C)	94	[46]
Pt/ZSM-5	0.2 %C_3H_8 + 2 %O_2/Ar	30,000	220	240	3.5(200 °C)	40	[47]
Pt-1 W/ZSM-5	0.2 %C_3H_8 + 2 %O_2/Ar	30,000	205	212	14.5(200 °C)	171	[47]
$NiCeO_x$-4	0.2 %C_3H_8 + 2 %O_2/Ar	30,000	275	300	14.5(250 °C)	0.33	[48]
10CoAl-400RO	0.1 %C_3H_8 + 18 %O_2/N_2	30,000	232	275	0.3(185 °C)	0.72	[49]
10CoAl-600RO	0.1 %C_3H_8 + 18 %O_2/N_2	30,000	216	257	11.5(185 °C)	5.43	[49]
Ca-Co_3O_4-Ac	0.2 %C_3H_8 + 5 %O_2/Ar	120,000	236	260	17.3(210 °C)	21.2	This work
Co_3O_4-Ac	0.2 %C_3H_8 + 5 %O_2/Ar	120,000	246	271	11.7(210 °C)	23.8	This work

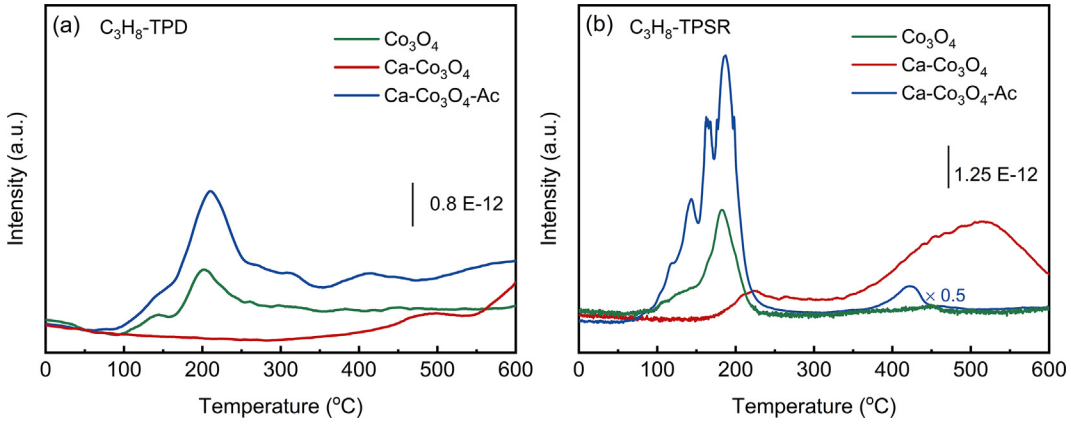

Fig. 7. (a) C_3H_8-TPD, and (b) C_3H_8-TPSR profiles of Co_3O_4, Ca-Co_3O_4, and Ca-Co_3O_4-Ac.

ciation into C_3H_7 and H and its corresponding free energy profile. The adsorption energy of C_3H_8 on pure Co_3O_4 was −0.42 eV, which was higher than the value of −0.47 eV computed for the $CaCO_3$-Co_3O_4 surface, but a little lower than the value of −0.36 eV for the $Ca_xCo_{3-x}O_4$ surface of Ca-Co_3O_4 sample. This indicated that the presence of $CaCO_3$ on the Co_3O_4 surface led to stronger adsorption of C_3H_8, while Ca incorporation into Co_3O_4 lattice resulted in weaker adsorption of C_3H_8 on the surface. Besides, the adsorption energy of C_3H_8 on Co_3O_4-D surface was −0.50 eV, nearly similar to that of $CaCO_3$-Co_3O_4, suggesting that the generation of active oxygen species also promoted C_3H_8 adsorption on the surface. However, the activation barrier for C_3H_8 dissociation on Co_3O_4-D surface was 0.43 eV, which was significantly lower than that of $CaCO_3$-Co_3O_4 (1.00 eV), Co_3O_4 (0.80 eV) and $Ca_xCo_{3-x}O_4$ (0.80 eV) surface. This difference inferred that more facile activation of C_3H_8 molecule on Ca-Co_3O_4-Ac sample than that on Co_3O_4 and Ca-Co_3O_4 samples, agreeing with the C_3H_8-TPD/TPSR results. From the DFT simulation, the active oxygen species originated from doping-etching strategy favors C_3H_8 adsorption and activation on Ca-Co_3O_4-Ac surface.

3.6. In-situ DRIFTS analysis

In-situ DRIFTS technique was used to identify the adsorbed species and the intermediates on the catalyst surface during the reaction process, and thus providing an insight into the effect of alkaline-earth metal doping and acid etching treatment on reaction mechanism. The in-situ DRIFT spectra of propane adsorption over the Co_3O_4, Ca-Co_3O_4 and Ca-Co_3O_4-Ac catalysts at 50 °C are shown in Fig. 9a. The bands at 2968 and 2980 cm^{-1} usually belonged to the C-H vibrations of gaseous C_3H_8, while the bands at 2902–2872 cm^{-1} were attributed to the C-H vibrations of CH, CH_2 or CH_3 species, indicating that propane was adsorbed and partially oxidatively cracked on the catalyst surface [4,54]. The bands around 3500/1626 and 3380 cm^{-1} were classified as ν(O-H) of isolated/ polymerized –OH groups or adsorbed water and intensified with exposure time [55]. In addition, multiple bands between 1000 and 1800 cm^{-1} appeared and gradually intensified with exposed time. Briefly, the bands at 1548, 1430, and 1350 cm^{-1} were assigned to ν_{as} (COO), ν_s (COO) and δ (CH_3) of acetate species. Other band at 1470, 1378 and 1290 cm^{-1} was attributed to δ_{as} (CH_3), δ_s (CH_3) and ν(C-O) groups, respectively. Meanwhile, carbonate species (1510 and 1420 cm^{-1}) and alkoxide species (<1156 cm^{-1}) were also identified during the propane adsorption [56]. This indicated that propane adsorbed on the catalyst was easy to be partially oxidized by labile oxygen. The formation of the intermediates over Ca-Co_3O_4-Ac was similar to that of Co_3O_4, whereas more carbonate species accumulated on the Ca-Co_3O_4 surface. This difference may be closely related to presence of surface $CaCO_3$ and active oxygen species.

After the adsorption of propane, 5 vol% O_2/Ar was introduced and the in-situ DRIFT spectra of all samples were recorded at the temperature of 50–300 °C. For Co_3O_4 sample (Fig. 9b), most of the characteristic bands tended to strengthen first and then

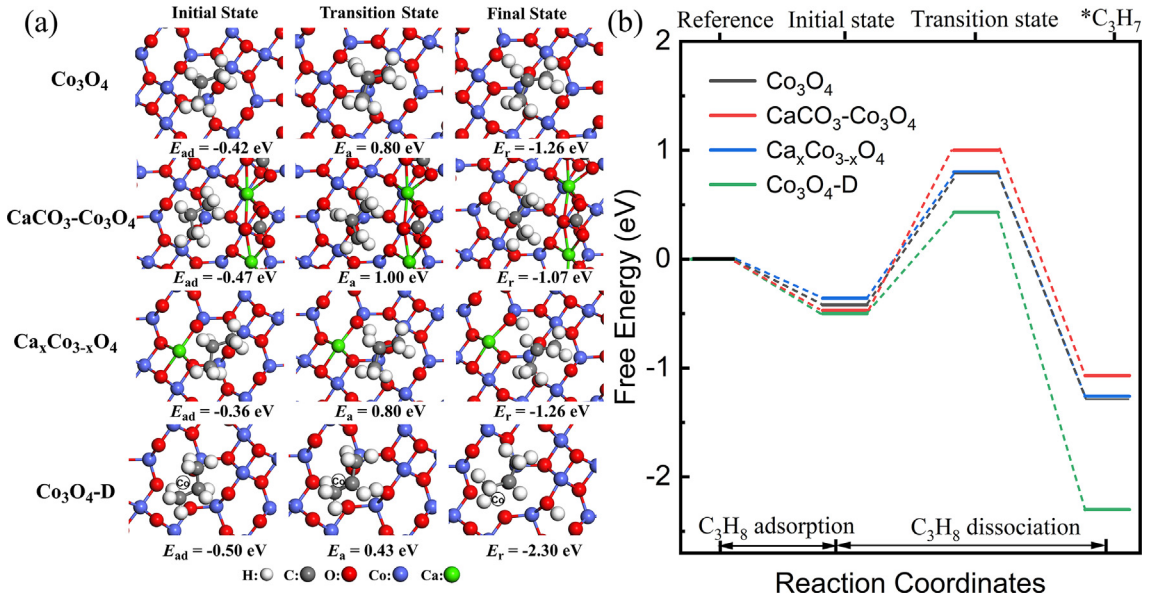

Fig. 8. (a) Heterolytic reaction paths for the first C-H bond activation of propane, and (b) the corresponding energy profile over Co_3O_4, Ca-Co_3O_4, and Ca-Co_3O_4-Ac catalyst.

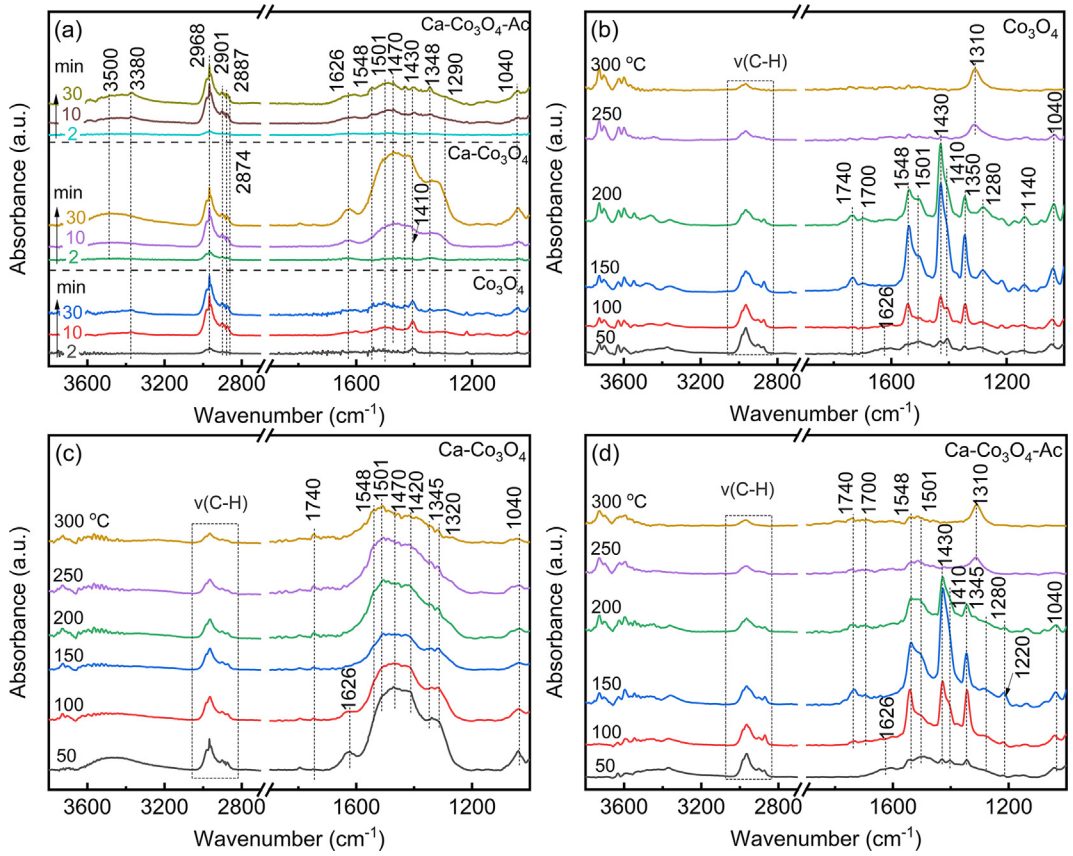

Fig. 9. In-situ DRIFT spectra of (a) propane adsorption (0.2 vol% C_3H_8/Ar) over Co_3O_4, Ca-Co_3O_4 and Ca-Co_3O_4-Ac samples at 50 °C, and propane oxidation (0.2 vol% C_3H_8, 5 vol % O_2/Ar) over (b) Co_3O_4, (c) Ca-Co_3O_4, and (d) Ca-Co_3O_4-Ac samples at 50–300 °C.

weaken with the temperature rising, indicating that gaseous oxygen supplemented the labile oxygen consumed on the catalyst surface and continued to react with propane. When the temperature was 150 °C, new adsorption peaks corresponding to the vibration of C = O bonds of acetone and aliphatic ester groups (1700 and 1740 cm^{-1}) appeared on the catalyst surface under the attack of labile oxygen, and these bands also increased first and then decreased throughout the reaction [57,58]. As the temperature rose to 250 and 300 °C, the bands of above-mentioned intermediates substantially disappeared, and new absorption bands attributed to unidentate carbonates appeared at 1310 cm^{-1} [59,60]. It implied that multiple pathways coexisted in propane oxidation

over the Co_3O_4 catalyst, in which unidentate carbonates may be the final intermediates and were converted to CO_2 eventually. However, the evolution process of above-mentioned functional groups over Ca-Co_3O_4 was different. As shown in Fig. 9c, more acetate and carbonate species (1501 cm^{-1}) accumulated on Ca-Co_3O_4 surface. Even at the reaction temperature of 300 °C, there were still some residual acetate and carbonates intermediate on the Ca-Co_3O_4 surface. It could be speculated that alkaline-earth metal doping promoted the accumulation of carbonates and carboxylate intermediates on the surface. In other words, alkaline-earth metal doping inhibited the transformation of the intermediates, which covered some active sites, thus reducing the catalytic activity. The evolution process of the intermediates over Ca-Co_3O_4-Ac was similar to that of Co_3O_4, except a trace of carboxylate species existing at 250 °C (Fig. 9d), which may be related to the residual alkaline-earth metals on the surface.

Based on the in-situ DRIFTS, C_3H_8-TPD/TPSR, and DFT calculation, the propane oxidation mechanism was proposed (Scheme 2). Although the alkaline-earth metals doping promoted the initial adsorption of C_3H_8 on the surface, but inhibited the further activation of C_3H_8, while the active oxygen species induced by doping-etching strategy not only promoted the C_3H_8 adsorption, but also accelerated the further activation of C_3H_8. In general, the complex reaction pathway can be described as follows: The gaseous C_3H_8 was firstly adsorbed on the active sites of catalyst surface, forming chemisorbed C_3H_{8-n}; Then, the activated C_3H_{8-n} reacted with the chemisorbed oxygen species to form alkoxide species, which easily converted to carboxylate and carbonates species. Meanwhile, as the reaction temperature rose, the intermediates such as acetone and aliphatic ester groups generated on the surface, which would be further oxidized to carbonate or carboxylate species. Finally, these intermediates were all oxidized into the final products CO_2 and H_2O.

3.7. Stability

Experimentally, thermal stability and water vapor resistance are essential to evaluate the catalyst for potential industrial applications. To achieve approximately equal initial propane conversion, the thermal stability tests of Ca-Co_3O_4 and Ca-Co_3O_4-Ac were performed at 280 and 260 °C, respectively. Both Co_3O_4 and Ca-Co_3O_4-Ac catalysts exhibited stable activity for propane oxidation during the tested 50 h (Fig. 10a), and their XRD crystallite phase remained unchanged after the stability test (Fig. S5). With 2.5 vol% water vapor introducing into feed gas, the propane conversion of Co_3O_4 and Ca-Co_3O_4-Ac slightly decreased, but they could restore to the original level after the remove of water vapor. All these indicated that Ca-Co_3O_4-Ac catalyst had a good stability and water vapor resistance comparable to Co_3O_4. Furthermore, Ca-Co_3O_4-Ac also exhibited a satisfactory cycle stability, and no

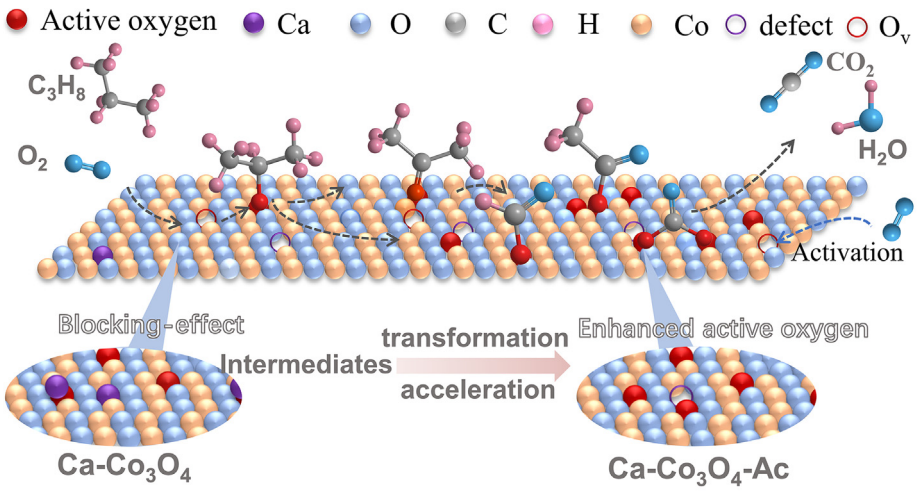

Scheme 2. Probable propane oxidation mechanism on M−Co_3O_4 and M−Co_3O_4−Ac catalysts.

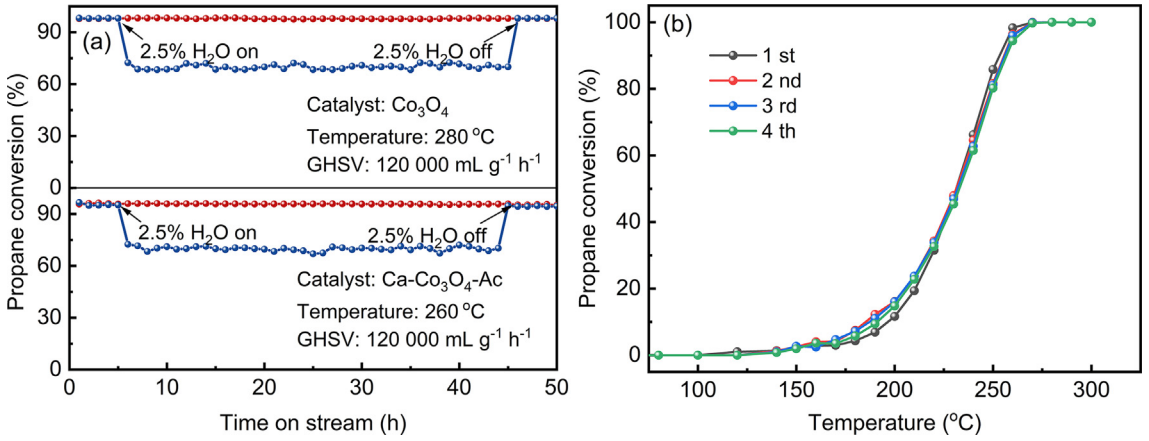

Fig. 10. (a) Thermal stability over Co_3O_4 at 280 °C and Ca-Co_3O_4-Ac at 260 °C under dry and humid conditions, and (b) Cyclic reusability of Ca-Co_3O_4-Ac catalyst for propane oxidation. (Reaction conditions: 100 mg catalyst, 0.2 vol% C_3H_8, 5 vol% O_2, balance Ar, and 2.5 vol% H_2O addition in humid condition. 120000 mL $g^{-1}h^{-1}$).

significant changes of the catalytic activity occurred after four cyclic experiments (Fig. 10b). These results further confirmed that Ca-Co_3O_4-Ac catalyst had a satisfactory hydrothermal stability and cycle stability, and doping-etching is a potential strategy for designing highly efficient catalyst for practical application in VOCs removal.

4. Conclusions

In summary, the doping-etching strategy significantly enhanced the catalytic performance of Co_3O_4 catalyst via the process of alkaline-earth metal doping and the subsequent acid etching treatment. The as-synthesized Ca-Co_3O_4-Ac catalyst exhibited the best catalytic performance, for which the T_{90} was 260 °C, 88 °C and 19 °C lower than that of Ca-Co_3O_4 and Co_3O_4 catalyst, respectively. Simultaneously, Ca-Co_3O_4-Ac showed high propane oxidation rate (5.65×10^{-7} mol g^{-1} s^{-1}) and TOF (2.12×10^{-3} s^{-1}) at 210 °C. Characterizations revealed the doping-etching strategy could increase the specific surface area, low-temperature reducibility, and oxygen mobility of Co_3O_4 catalyst, thus promoting the catalytic activity of the M−Co_3O_4−Ac catalyst. In-situ DRIFTS, DFT calculation, and C_3H_8-TPD/TPSR analysis further revealed that active lattice oxygen species induced by doping-etching strategy promoted the propane activation on the surface. In addition, Ca-Co_3O_4-Ac showed excellent long-term stability and reusability in the presence of 2.5 vol% H_2O. This work offers a deeper understanding of the reactive oxygen species, and provides a doping-etching strategy to effectively improve the catalytic performance of Co_3O_4 catalyst in practical VOCs removal, which can also be generalized for the development of other transition metal oxides.

CRediT authorship contribution statement

Wenjun Zhu: Conceptualization, Methodology, Writing – original draft. **Xing-bao Wang:** Software. **Chuang Li:** Supervision, Validation. **Xiao Chen:** Supervision, Validation. **Wen-ying Li:** Software. **Zhongmin Liu:** Validation, Resources. **Changhai Liang:** Validation, Resources.

Declaration of Competing Interest

The authors declare that they have no known competing financial interests or personal relationships that could have appeared to influence the work reported in this paper.

Acknowledgements

We gratefully acknowledge the financial support provided by the Liaoning Revitalization Talent Program (XLYC1908033) and the Fundamental Research Funds for the Central Universities (DUT2021TB03).

Appendix A. Supplementary material

Supplementary data to this article can be found online at https://doi.org/10.1016/j.jcat.2022.06.024.

References

[1] H. Huang, Y. Xu, Q. Feng, D.Y.C. Leung, Low temperature catalytic oxidation of volatile organic compounds: a review, Catal. Sci. Technol. 5 (2015) 2649–2669.
[2] B. Liu, J. Ji, B. Zhang, W. Huang, Y. Gan, D.Y.C. Leung, H. Huang, Catalytic ozonation of VOCs at low temperature: A comprehensive review, J. Hazard. Mater. 422 (2021) 126847.
[3] C. He, J. Cheng, X. Zhang, M. Douthwaite, S. Pattisson, Z. Hao, Recent Advances in the Catalytic Oxidation of Volatile Organic Compounds: A Review Based on Pollutant Sorts and Sources, Chem. Rev. 119 (2019) 4471–4568.
[4] T. Zhang, X. Lang, A. Dong, X. Wan, S. Gao, L. Wang, L. Wang, W. Wang, Difference of oxidation mechanism between light C3–C4 alkane and alkene over mullite YMn_2O_5 oxides catalyst, ACS Catal. 10 (2020) 7269–7282.
[5] K. Li, J. Ji, M. He, H. Huang, Complete oxidation of formaldehyde over Pd/CeO_2 catalyst at room temperature: Tunable active oxygen species content by non-thermal plasma activation, Catal. Sci. Technol. 10 (2020) 6257–6265.
[6] E. García-López, G. Marcì, F. Puleo, V. La Parola, L.F. Liotta, $La_{1-x}Sr_xCo_{1-y}Fe_yO_{3-\delta}$ perovskites: Preparation, characterization and solar photocatalytic activity, Appl. Catal. B: Environ. 178 (2015) 218–225.
[7] W. Zhu, X. Chen, Z. Liu, C. Liang, Insight into the Effect of Cobalt Substitution on the Catalytic Performance of $LaMnO_3$ Perovskites for Total Oxidation of Propane, J. Phys. Chem. C 124 (2020) 14646–14657.
[8] C. Wang, Y. Li, C. Zhang, X. Chen, C. Liu, W. Weng, W. Shan, H. He, A simple strategy to improve Pd dispersion and enhance Pd/TiO_2 catalytic activity for formaldehyde oxidation: The roles of surface defects, Appl. Catal. B: Environ. 282 (2021) 119540.
[9] X. Ma, Y. Tang, Y. Liu, Y. Zhang, L. Jia, X. Liu, C. Du, B. Shan, A-site cation exfoliation of amorphous $SmMn_xO_y$ oxides for low temperature propane oxidation, J. Catal. 409 (2022) 59–69.
[10] C.P. O'Brien, G.R. Jenness, H. Dong, D.G. Vlachos, I.C. Lee, Deactivation of Pt/Al_2O_3 during propane oxidation at low temperatures: Kinetic regimes and platinum oxide formation, J. Catal. 337 (2016) 122–132.
[11] Z. Wang, Z. Huang, J.T. Brosnahan, S. Zhang, Y. Guo, Y. Guo, L. Wang, Y. Wang, W. Zhan, Ru/CeO_2 Catalyst with Optimized CeO_2 Support Morphology and Surface Facets for Propane Combustion, Environ. Sci. Technol. 53 (2019) 5349–5358.
[12] J. Dong, D. Li, Y. Zhang, P. Chang, Q. Jin, Insights into the CeO_2 facet-depended performance of propane oxidation over Pt-CeO_2 catalysts, J. Catal. 407 (2022) 174–185.
[13] W. Tang, W. Xiao, S. Wang, Z. Ren, J. Ding, P.-X. Gao, Boosting catalytic propane oxidation over PGM-free Co_3O_4 nanocrystal aggregates through chemical leaching: A comparative study with Pt and Pd based catalysts, Appl. Catal. B: Environ. 226 (2018) 585–595.
[14] L.F. Liotta, H. Wu, G. Pantaleo, A.M. Venezia, Co_3O_4 nanocrystals and Co_3O_4–MO_x binary oxides for CO, CH_4 and VOC oxidation at low temperatures: a review, Catal. Sci. Technol. 3 (2013) 3085–3102.
[15] Z. Guo, B. Liu, Q. Zhang, W. Deng, Y. Wang, Y. Yang, Recent advances in heterogeneous selective oxidation catalysis for sustainable chemistry, Chem. Soc. Rev. 43 (2014) 3480–3524.
[16] Q. Ren, S. Mo, R. Peng, Z. Feng, M. Zhang, L. Chen, M. Fu, J. Wu, D. Ye, Controllable synthesis of 3D hierarchical Co_3O_4 nanocatalysts with various morphologies for the catalytic oxidation of toluene, J. Mater. Chem. A 6 (2018) 498–509.
[17] W. Zhu, X. Chen, C. Li, Z. Liu, C. Liang, Manipulating morphology and surface engineering of spinel cobalt oxides to attain high catalytic performance for propane oxidation, J. Catal. 396 (2021) 179–191.
[18] S. Mo, Q. Zhang, Y. Sun, M. Zhang, J. Li, Q. Ren, M. Fu, J. Wu, L. Chen, D. Ye, Gaseous CO and toluene co-oxidation over monolithic core-shell Co_3O_4-based hetero-structured catalysts, J. Mater. Chem. A 27 (2019) 16197–16210.
[19] L. Hu, Q. Peng, Y. Li, Selective Synthesis of Co_3O_4 Nanocrystal with Different Shape and Crystal Plane Effect on Catalytic Property for Methane Combustion, J. Am. Chem. Soc. 130 (2008) 16136–16137.
[20] H.-F. Wang, R. Kavanagh, Y.-L. Guo, Y. Guo, G. Lu, P. Hu, Origin of extraordinarily high catalytic activity of Co_3O_4 and its morphological chemistry for CO oxidation at low temperature, J. Catal. 296 (2012) 110–119.
[21] W. Zhu, X. Chen, J. Jin, X. Di, C. Liang, Z. Liu, Insight into catalytic properties of Co_3O_4-CeO_2 binary oxides for propane total oxidation, Chin. J. Catal. 41 (2020) 679–690.
[22] G. Chai, W. Zhang, L.F. Liotta, M. Li, Y. Guo, A. Giroir-Fendler, Total oxidation of propane over Co_3O_4-based catalysts: Elucidating the influence of Zr dopant, Appl. Catal. B: Environ. 298 (2021) 120606.
[23] Y. Jian, M. Tian, C. He, J. Xiong, Z. Jiang, H. Jin, L. Zheng, R. Albilali, J.-W. Shi, Efficient propane low-temperature destruction by Co_3O_4 crystal facets engineering: Unveiling the decisive role of lattice and oxygen defects and surface acid-base pairs, Appl. Catal. B: Environ. 283 (2021) 119657.
[24] W. Zhang, K. Lassen, C. Descorme, J.L. Valverde, A. Giroir-Fendler, Effect of the precipitation pH on the characteristics and performance of Co_3O_4 catalysts in the total oxidation of toluene and propane, Appl. Catal. B: Environ. 282 (2021) 119566.
[25] W. Si, Y. Wang, Y. Peng, J. Li, Selective Dissolution of A-Site Cations in ABO_3 Perovskites: A New Path to High-Performance Catalysts, Angew. Chem. Int. Edit. 54 (2015) 7954–7957.
[26] W. Si, Y. Wang, S. Zhao, F. Hu, J. Li, A Facile Method for in Situ Preparation of the MnO_2/$LaMnO_3$ Catalyst for the Removal of Toluene, Environ. Sci. Technol. 50 (2016) 4572–4578.
[27] Q. Yang, D. Wang, C. Wang, X. Li, K. Li, Y. Peng, J. Li, Facile surface improvement method for $LaCoO_3$ for toluene oxidation, Catal. Sci. Technol. 8 (2018) 3166–3173.
[28] C. Reed, Y.-K. Lee, S.T. Oyama, Structure and Oxidation State of Silica-Supported Manganese Oxide Catalysts and Reactivity for Acetone Oxidation with Ozone, J. Phys. Chem. B 110 (2006) 4207–4216.

[29] Y. Qin, H. Wang, C. Dong, Z. Qu, Evolution and enhancement of the oxygen cycle in the catalytic performance of total toluene oxidation over manganese-based catalysts, J. Catal. 380 (2019) 21–31.
[30] S. Oyama, X. Zhang, J. Lu, Y. Gu, T. Fujitani, Epoxidation of propylene with H_2 and O_2 in the explosive regime in a packed-bed catalytic membrane reactor, J. Catal. 257 (2008) 1–4.
[31] X.-B. Wang, Z.-Z. Xie, L. Guo, Z.-Y. Du, W.-Y. Li, Mechanism of Dibenzofuran Hydrodeoxygenation on the Surface of Pt(111): A DFT Study, Catal. Today 364 (2021) 220–228.
[32] K. Chen, W. Li, Z. Zhou, Q. Huang, Y. Liu, Q. Duan, Hydroxyl groups attached to Co^{2+} on the surface of Co_3O_4: a promising structure for propane catalytic oxidation, Catal. Sci. Technol. 10 (2020) 2573–2582.
[33] W. Liu, R. Liu, X. Zhang, Controllable synthesis of 3D hierarchical Co_3O_4 catalysts and their excellent catalytic performance for toluene combustion, Appl. Surf. Sci. 507 (2019) 145174.
[34] Y. Sun, J. Xu, X. Xu, X. Fang, Y. Guo, R. Liu, W. Zhong, X. Wang, Tailoring Active O^{2-} and O_2^{2-} Anions on a ZnO Surface with the Addition of Different Alkali Metals Probed by CO Oxidation, Ind. Eng. Chem. Res. 59 (2020) 9382–9392.
[35] Y. Su, K. Fu, Y. Zheng, N. Ji, C. Song, D. Ma, X. Lu, R. Han, Q. Liu, Catalytic oxidation of dichloromethane over Pt-Co/HZSM-5 catalyst: Synergistic effect of single-atom Pt, Co_3O_4, and HZSM-5, Appl. Catal. B: Environ. 288 (2021) 119980.
[36] W. Tang, J. Weng, X. Lu, L. Wen, A. Suburamanian, C.-Y. Nam, P.-X. Gao, Alkali-Metal Poisoning Effect of Total CO and Propane Oxidation over Co_3O_4 Nanocatalysts, Appl. Catal. B: Environ. 256 (2019) 117859.
[37] R. Li, Y. Huang, D. Zhu, W. Ho, J. Cao, S. Lee, Improved Oxygen Activation over a Carbon/Co_3O_4 Nanocomposite for Efficient Catalytic Oxidation of Formaldehyde at Room Temperature, Environ. Sci. Technol. 55 (2021) 4054–4063.
[38] Y. Zheng, R. Zhang, L. Zhang, Q. Gu, Z.-A. Qiao, A Resol-assisted Cationic Coordinative Co-assembly Approach to Mesoporous ABO_3 Perovskite Oxides with Rich Oxygen Vacancy for Enhanced Hydrogenation of Furfural to Furfuryl Alcohol, Angew. Chem. Int. Ed. 60 (2021) 4774–4781.
[39] N.A. Merino, B.P. Barbero, P. Eloy, L.E. Cadús, $La_{1-x}Ca_xCoO_3$ perovskite-type oxides: Identification of the surface oxygen species by XPS, Appl. Surf. Sci. 253 (2006) 1489–1493.
[40] Y. Cai, J. Xu, Y. Guo, J. Liu, Ultrathin, Polycrystalline, Two-Dimensional Co_3O_4 for Low-Temperature CO Oxidation, ACS Catal. 9 (2019) 2558–2567.
[41] L. Zhang, L. Shi, L. Huang, J. Zhang, R. Gao, D. Zhang, Rational Design of High-Performance DeNO$_x$ Catalysts Based on $Mn_xCo_{3-x}O_4$ Nanocages Derived from Metal-Organic Frameworks, ACS Catal. 4 (2014) 1753–1763.
[42] W. Sun, B. Gong, J. Pan, Y. Wang, H. Xia, H. Zhang, Q. Dai, L. Wang, X. Wang, Catalytic combustion of CVOCs over Cr_xTi_{1-x} oxide catalysts, J. Catal. 391 (2020) 132–144.
[43] R. Vidruk, M.V. Landau, M. Herskowitz, M. Talianker, N. Frage, V. Ezersky, N. Froumin, Grain boundary control in nanocrystalline MgO as a novel means for significantly enhancing surface basicity and catalytic activity, J. Catal. 263 (2009) 196–204.
[44] N. Miniajluk, J. Trawczyński, M. Zawadzki, Properties and catalytic performance for propane combustion of $LaMnO_3$ prepared under microwave-assisted glycothermal conditions: Effect of solvent diols, Appl. Catal. A: Gen. 531 (2017) 119–128.
[45] P. Zhao, X. Li, W. Liao, Y. Wang, J. Chen, J. Lu, M. Luo, Understanding the Role of NbO$_x$ on Pt/Al_2O_3 for Effective Catalytic Propane Oxidation, Ind. Eng. Chem. Res. 58 (2019) 21945–21952.
[46] K. Baranowska, J. Okal, Performance and Stability of the Ru–Re/γ-Al_2O_3 Catalyst in the Total Oxidation of Propane: Influence of the Order of Impregnation, Catal. Lett. 146 (2015) 72–81.
[47] Z. Zhu, G. Lu, Y. Guo, Y. Guo, Z. Zhang, Y. Wang, X.-Q. Gong, High Performance and Stability of the Pt-W/ZSM-5 Catalyst for the Total Oxidation of Propane: The Role of Tungsten, ChemCatChem 5 (2013) 2495–2503.
[48] Z. Hu, S. Qiu, Y. You, Y. Guo, Y. Guo, L. Wang, W. Zhan, G. Lu, Hydrothermal synthesis of NiCeO$_x$ nanosheets and its application to the total oxidation of propane, Appl. Catal. B: Environ. 225 (2017) 110–120.
[49] T. Cai, W. Deng, P. Xu, J. Yuan, Z. Liu, K. Zhao, Q. Tong, D. He, Great activity enhancement of Co_3O_4/γ-Al_2O_3 catalyst for propane combustion by structural modulation, Chem. Eng. J. 395 (2020) 125071.
[50] N.W. Cant, C.A. Lukey, P.F. Nelson, R.J. Tyler, The rate controlling step in the oxidative coupling of methane over a lithium-promoted magnesium oxide catalyst, J. Chem. Soc., Chem. Commun. 12 (1988) 766–768.
[51] J. Wei, E. Iglesia, Isotopic and kinetic assessment of the mechanism of methane reforming and decomposition reactions on supported iridium catalysts, Phys. Chem. Chem. Phys. 6 (2004) 3754–3759.
[52] G. Jones, J.G. Jakobsen, S.S. Shim, J. Kleis, M.P. Andersson, J. Rossmeisl, F. Abild-Pedersen, T. Bligaard, S. Helveg, B. Hinnemann, J.R. Rostrup-Nielsen, I. Chorkendorff, J. Sehested, J.K. Nørskov, First principles calculations and experimental insight into methane steam reforming over transition metal catalysts, J. Catal. 259 (2008) 147–160.
[53] E.C. Tyo, C. Yin, M. Di Vece, Q. Qian, G. Kwon, S. Lee, B. Lee, J.E. DeBartolo, S. Seifert, R.E. Winans, R. Si, B. Ricks, S. Goergen, M. Rutter, B. Zugic, M. Flytzani-Stephanopoulos, Z.W. Wang, R.E. Palmer, M. Neurock, S. Vajda, Oxidative Dehydrogenation of Cyclohexane on Cobalt Oxide (Co_3O_4) Nanoparticles: The Effect of Particle Size on Activity and Selectivity, ACS Catal. 2 (2012) 2409–2423.
[54] Z. Hu, X. Liu, D. Meng, Y. Guo, Y. Guo, G. Lu, Effect of Ceria Crystal Plane on the Physicochemical and Catalytic Properties of Pd/Ceria for CO and Propane Oxidation, ACS Catal. 6 (2016) 2265–2279.
[55] W. Yang, Y. Peng, Y. Wang, Y. Wang, H. Liu, Z.a. Su, W. Yang, J. Chen, W. Si, J. Li, Controllable Redox-induced In-situ Growth of MnO_2 over Mn_2O_3 for Toluene Oxidation: Active Heterostructure Interfaces, Appl. Catal. B: Environ., 278 (2020) 119279.
[56] F. Liu, J. Shen, D. Xu, W. Zhou, S. Zhang, L. Wan, Oxygen vacancies enhanced HCHO oxidation on a novel $NaInO_2$ supported Pt catalyst at room temperature, Chem. Eng. J. 334 (2018) 2283–2292.
[57] H. Kareem, S. Shan, Z.-P. Wu, L. Velasco, K. Moseman, C.P. O'Brien, D.T. Tran, I.C. Lee, Y. Maswadeh, L. Yang, D. Mott, J. Luo, V. Petkov, C.-J. Zhong, Catalytic oxidation of propane over palladium alloyed with gold: an assessment of the chemical and intermediate species, Catal, Sci. Technol. 8 (2018) 6228–6240.
[58] C.P. O'Brien, I.C. Lee, A detailed spectroscopic analysis of the growth of oxy-carbon species on the surface of Pt/Al_2O_3 during propane oxidation, J. Catal. 347 (2017) 1–8.
[59] R. Kang, X. Wei, F. Bin, Z. Wang, Q. Hao, B. Dou, Reaction mechanism and kinetics of CO oxidation over a CuO/$Ce_{0.75}Zr_{0.25}O_{2-\delta}$ catalyst, Appl. Catal. A: Gen. 565 (2018) 46–58.
[60] J. Wang, P. Zhang, J. Li, C. Jiang, R. Yunus, J. Kim, Room-Temperature Oxidation of Formaldehyde by Layered Manganese Oxide: Effect of Water, Environ. Sci. Technol. 49 (2015) 12372–12379.